Effects of thermal treatments on microstructure and mechanical properties of a Co-Cr-Mo-W biomedical alloy produced by laser sintering

Effects of thermal treatments on microstructure and mechanical properties of a Co-Cr-Mo-W biomedical alloy produced by laser sintering

P. Mengucci[1]*, G. Barucca[1], A. Gatto[2], E. Bassoli[2], L. Denti[2], F. Fiori[3], E. Girardin[3], P. Bastianoni[1], B. Rutkowski[4], A. Czyrska-Filemonowicz[4]

[1] Dipartimento SIMAU, Università Politecnica delle Marche, 60131 Ancona, Italy.

[2] Dipartimento DIEF, Università di Modena e Reggio Emilia, Via Vivarelli 10, 41125 Modena, Italy.

[3] Dipartimento DISCO, Università Politecnica delle Marche, 60131 Ancona, Italy.

[4] International Centre of Electron Microscopy for Material Science & Faculty of Metals Engineering and Industrial Computer Science, AGH University of Science and Technology, Al. A. Mickiewicza 30, 30-059 Kraków, Poland.

*** Corresponding author:**

Paolo Mengucci
Dip. SIMAU, Università Politecnica delle Marche
I-60131 Ancona
Italy
E-mail: p.mengucci@univpm.it

Abstract

Direct Metal Laser Sintering (DMLS) technology based on a layer by layer production process was used to produce a Co-Cr-Mo-W alloy specifically developed for biomedical applications. The alloy mechanical response and microstructure were investigated in the as-sintered state and after post-production thermal treatments. Roughness and hardness measurements, and tensile and flexural tests were performed to study the mechanical response of the alloy while X-ray diffraction (XRD), electron microscopy (SEM, TEM, STEM) techniques and microanalysis (EDX) were used to investigate the microstructure in different conditions. Results showed an intricate network of ε-Co (hcp) lamellae in the γ-Co (fcc) matrix responsible of the high UTS and hardness values in the as-sintered state. Thermal treatments increase volume fraction of the ε-Co (hcp) martensite but slightly modify the average size of the lamellar structure. Nevertheless, thermal treatments are capable of producing a sensible increase in UTS and hardness and a strong reduction in ductility. These latter effects were mainly attributed to the massive precipitation of an hcp $Co_3(Mo,W)_2Si$ phase and the contemporary formation of Si-rich inclusions.

Keywords: Co alloys; laser sintering; heat treatments; mechanical properties; structure characterisation.

1. Introduction

In medical applications such as knee and hip joint replacement, Co alloys are widely used due to biocompatibility, high strength, excellent wear and corrosion resistance (Balagna et al. 2012; Hiromoto et al. 2005; Saldivar-Garcia and Lopez 2005; Yamanaka et al. 2013). In dentistry, Co alloys are used in the production of metal frames, porcelain fused to metal (PFM) crowns and removable partial dentures (Craig et al. 2004; Yamanaka et al. 2015; Wataha 2002).

Generally, in the conventional production processes based on casting, plastic deformation and cutting the physical and mechanical properties of the Co alloys, such as high melting point, limited ductility and high hardness values, may constitute factors that increase the total cost of the biomedical devices. On the other hand, proper operation and long life expectancy of biomedical devices require biocompatibility, good mechanical properties and high corrosion resistance. Proposed solutions to these problems concern the manufacturing technology. In particular, additive manufacturing (AM) technologies based on a layer-by-layer production process assisted by a computer aided design (CAD) software are receiving growing attention (Harris 2012; Mumtaz et al. 2008; Stamp et al. 2009; Ucar et al. 2009).

Direct metal laser sintering (DMLS, Power Bed Fusion according to ASTM F42 committee) is an AM technology based on a laser beam that locally melts a metal powder according to the CAD model (Bassoli et al. 2013; Simchi 2006). The DMLS technology allows obtaining finished devices in a single production process, thus contributing to save time and improve efficiency. Furthermore, DMLS is particularly suitable for prosthetic applications in orthopaedics and dentistry where complex geometries, low volumes and strong individualization are required.

At times, there is a lack of knowledge regarding the mechanical performances of components produced by laser sintering due to the complex physical processes associated to laser sintering that include heat transfer and melting of powder (Simchi 2006). In other observations, parts produced by DMLS are even stronger than obtained by traditional processes, but they may suffer from lower reliability (Bassoli et al. 2013; Frazier 2014). In general, AM generates highly distinctive

microstructures, very dissimilar to those observed elsewhere, which turns into an urgent need for better knowledge of the expected performances.

High surface roughness, porosity, heterogeneous microstructure and thermal residual stresses are typically the most limiting problems that may affect the sintered products (Bassoli et al. 2012; Simchi 2006). In many cases, improvement of the mechanical response was obtained by post-production treatments (Balagna et al. 2012; Giacchi et al. 2011, 2012; Saldivar-Garcia et al. 1999a; Sanz and Navas 2013; Yamanaka et al. 2015; Zangeneh et al. 2010). Nevertheless, the development of high-strength materials is still the basic requirement for biomedical applications of Co alloys. Typically, a strength increase results in an improved mechanical behaviour of biomedical devices based on Co alloys (Lu et al. 2015; Takaichi et al. 2013; Yoda et al. 2012).

Several papers in literature report on the problem of biocompatibility of Co-based materials produced by conventional and AM techniques mainly because the corrosion susceptibility and the extent of metal release strongly depend on the alloy microstructure developed during the fabrication procedure or after post-production treatments (Antunes et al. 2012; Hedberg et al. 2014; Madl et al. 2015; Mostardi et al. 2010; Xin et al. 2012).

Post-production treatments can be quite complex as for example in dental applications where for aesthetic reasons restorations are veneered with dental porcelain in a firing process that include heating and cooling cycles. The heating temperatures in the firing cycle for Co alloys can reach values as high as 950 °C causing possible microstructural modifications of the material (Al Jabbari et al. 2014; Xin et al. 2014).

Although a large body of published papers is present in literature dealing with problems linked to applications of laser sintered Co alloys to the production of biomedical devices, a limited number of information are available on the structural modifications induced by post-production treatments performed to improve the alloy mechanical response and corrosion resistance.

In this study, a Co-Cr-Mo-W alloy specifically developed for biomedical applications was produced by the DMLS technology. After production, the alloy was submitted to shot-peening, stress relieving and firing cycle in order to simulate a complex post-production treatment.

Mechanical tests and structural characterisation were carried out on as-sintered samples as well as on samples submitted to post-production treatments. Results of the structural characterisation performed on the as-sintered sample were already published in a previous paper (Barucca et al. 2015). In this paper, results obtained from tensile and flexural tests on the post-processed samples are discussed in function of the structural properties of the alloy investigated by X-ray diffraction (XRD), scanning electron microscopy (SEM), transmission and scanning transmission electron microscopy (TEM, STEM) and energy dispersive X-ray microanalysis (EDX). Results evidenced strong modifications of microstructure and mechanical behaviour of the alloy as a consequence of the post-production treatments. In particular, changes in the mechanical response were mainly correlated to the formation and growth of coarse and elongated precipitates induced by the post-production treatment. To our best knowledge, the presence of coarse and elongated precipitates is reported here for the first time.

2. Material and methods

2.1 Material composition and sintering parameters

EOS CobaltChrome SP2 powder was submitted to the action of a laser beam in the EOSINT M270 system to produce flexural and tensile specimens by using the standard sintering parameters shown in Table 1.

Table 1 about here

The material is a Co-Cr-Mo-W alloy (Type 4 according to standard DIN EN ISO 22674:2006) for biomedical applications. The nominal powder composition provided by the manufacturer (EOS

GmbH Electro Optical System) is reported in Table 2. The powder is free of Ni, Be and Cd in accordance to EN ISO 22674.

Table 2 about here

Material properties claimed by the producer after stress relieving (see the complete sequence of the thermal stress relieving treatment reported below), oxide fire simulation (5 min. at 950 °C) and ceramic fire simulation (4 x 2 min. at 930 °C) procedures according to EN ISO 22674, are listed in Table 3.

Table 3 about here

2.2 Thermal treatments and mechanical tests

Flexural specimens (FLEX) were produced according to ASTM B528-05 (Standard Test Method for Transverse Rupture Strength of Metal Powder Specimens) and B 925–08 (Standard Practices for Production and Preparation of Powder Metallurgy (PM) Test Specimens).

Tensile specimens (TENS) were built following ASTM E8M:11 (Standard Test Methods for Tension Testing of Metallic Materials).

Figure 1 shows geometry and dimensions of FLEX (Figure 1a) and TENS (Figure 1b) samples, respectively. In both drawings, Z is the direction of growth in the AM machine, and XY is the plane of powder deposition; X is the slide direction of the recoater.

Figure 1 about here

After additive fabrication, parts were shot-peened following the datasheet recommendations, using fine spherical ceramic media (70% ZrO_2 - 30% SiO_2, 125 - 250µm), at 3 bar pressure. Shot-peening

produces a compressive residual stress layer (Sanz and Navas 2013). A thermal stress relieving treatment was then performed under argon atmosphere, with the following sequence:

- Heat furnace to 450 °C in 60 minutes.
- Hold temperature for 45 minutes.
- Heat furnace to 750 °C in 45 minutes.
- Hold temperature for 60 minutes.
- Switch furnace heating off. When temperature dropped down to approx. 600 °C, open the furnace door.

From now on, the stress relieving thermal treatment just described above is referred to as RHT.

In dental restorations, after the RHT process the metal structure is then veneered with dental ceramic material during a firing operation, which includes five steps.

The standard five-steps firing cycle, compliant to EN ISO 22674, adopted in this work for the samples already submitted to the RHT process, is outlined in Figure 2. Starting from a pre-heating temperature of 450 °C, five steps simulate the firing of oxide and ceramic layers.

From now on, samples or groups of samples submitted to both the RHT treatment and the firing cycle are labelled as CHT.

Figure 2 about here

In order to evaluate the effects of the stress relieving heat treatment (RHT) and the firing cycle (CHT) on mechanical properties and microstructure of the investigated alloy, a number of tensile (TENS) and flexural (FLEX) specimens in different conditions were studied. For each condition a number of 6 samples were investigated. The sample group in the as-sintered (AS) condition was named $TENS_{AS}$.

Details of the mechanical tests performed on the different groups of samples are summarised in the following:

- Tensile tests (crosshead speed 5 mm/min, load cell capacity 250 kN);

- Three point bending tests (support width 25.4 mm, crosshead speed 2 mm/min, load cell capacity 30 kN).

Although it is known that parts are weaker when built in the Z direction, we decided to measure the performances in X direction because that reproduces the orientation in which dental structures are built. Any dental prostheses, for example a bridge, would be laid in the XY plane, in order to reduce building time and costs and to allow for optimal support positioning. Therefore, the bridge can be considered as a beam built along the X-axis, or in the XY plane without substantial changes, and subject to flexure. Possible variation of the mechanical properties with specimen orientation cannot be excluded.

2.3 Hardness measurements

Based on the recommendations of ISO 4498:2010 (Sintered metal materials, excluding hard metals -- Determination of apparent hardness and microhardness), Rockwell A hardness test was chosen, and performed by means of an ERNST NR3D Hardness tester, following the specifications of ISO 6508-1:2015 (Metallic materials -- Rockwell hardness test).

2.4 Roughness measurements

Roughness measurements adhering to EN 10049:2013 were carried out by means of a DIAVITE DH-5 stylus tester, by adopting a travel length l_t of 4.8 mm, with a cut-off filter of 0.8 mm, giving an evaluation length l_m of 4 mm. Five measurements per sample were recorded for statistical reasons, taken on XZ faces along the X direction. The standard deviations (SD) associated to the roughness value were estimated from the five measurements.

2.4 Statistical tests

Statistical tests were performed in order to assess whether the heat treatments cause significant changes in the mechanical response. Possible significant differences between the groups were

checked by means of the t-test for independent samples by using a software tool for statistical analysis (Statistica 8, Statsoft). The test can be used to determine if two sets of data are significantly different from each other. It results in probability values (p-values): when lower than 0.05 they can be taken as a decision to reject the null hypothesis of equality between two groups of samples. In this study, when for example tensile strengths of $TENS_{AS}$ and $TENS_{RHT}$ are compared by means of a t-test, a p-value lower than 0.05 allows rejecting the hypothesis that the relief treatment leaves strength unchanged, that is to say it allows to admit a significant effect of the heat treatment on strength.

2.5 Structural characterisation

Rupture surfaces of one sample per group were observed by an environmental scanning electron microscope (ESEM) FEI Quanta 200, operating in low-vacuum mode (0.5 Torr) at 25 kV to relate the mechanical properties to failure mechanisms in the micro-scale

Furthermore, in order to correlate the mechanical behaviour of the several sample groups to the microstructure developed during the production process and the different thermal treatments, two groups of samples were structurally characterized. The first group (named AS) was in the as sintered condition, while samples belonging to the second group (named CHT) were firstly submitted to the stress relieving treatment and then to the firing cycle. Independently on the sample group (AS or CHT), samples structurally characterised by the analytical techniques listed below, were not submitted to either tensile or flexural mechanical tests.

Structural characterizations were carried out by X-ray diffraction (XRD), transmission (TEM) and scanning transmission (STEM) electron microscopy techniques and energy dispersive X-ray microanalysis (EDX).

For XRD measurements a Bruker D8 Advance diffractometer operating at V= 40kV and I= 40 mA in the angular range 2θ=10 - 80° was used. XRD measurements were carried out by Cu-Kα radiation. TEM analyses were performed by a Philips CM200 electron microscope and JEOL JEM-2010 ARP microscope equipped with an Oxford Inca energy dispersive X-ray microanalysis, both operating at

200 kV. Analytical high resolution microscopy was conducted by a probe Cs-corrected FEI Titan^3 G2 60-300 equipped with ChemiSTEM technology (X-FEG field-emission gun and Super-X EDX detector system) developed at FEI (FEI application note AN002707-2010. Available from: www.fei.com).

TEM bright-field imaging and STEM imaging using high-angle annular-dark-field (HAADF) contrast as well as EDX mapping and high resolution TEM (HRTEM) imaging were used for characterization of the samples micro/nanostructure and chemical composition of phases down to the nano-scale. Phase identification was performed by selected area electron diffraction (SAED), STEM-EDX and fast Fourier transform (FFT) of HRTEM images. The diffraction patterns and HRTEM images were interpreted with the JEMS software (Stadelman 2007).

Samples for TEM observations were mechanically prepared by grinding on abrasive papers and diamond pastes. Disks with a 3 mm diameter were cut from the bulk material by an ultrasonic cutter (Gatan). In order to reduce time of ion milling, in the last step of the mechanical thinning procedure, each 3 mm disk was mechanically thinned in a central area by a Dimple Grinder (Gatan). Final thinning was carried out by an ion beam system (Gatan PIPS) using Ar ions at 5 kV.

Samples (lamellae) for STEM, HRTEM and EDX analyses were prepared by Focused Ion Beam (FIB) technique by the ZEISS NEON CrossBeam 40EsB microscope. Before milling, a layer of Pt was deposited at the place of cutting in order to protect the thin sample against heavy Ga ions during the preparation. Final milling was performed with the 4 keV Ga+ beam.

3. Results

3.1 Roughness measurements

Roughness measurements provided values in the same range for all the specimens. The average value of the roughness R_a was 2.2 µm, with a standard deviation (SD) of 0.4 µm. As maximum roughness R_{max}, an average value of 15 µm (SD = 2 µm) was obtained.

3.2 Hardness and mechanical tests

The results of tensile and hardness tests on the tensile specimens are shown in Table 4, separately for the different groups ($TENS_{AS}$, $TENS_{RHT}$, $TENS_{CHT}$). The average value (AV) is reported with the corresponding standard deviation (SD). Tensile strength just after building ($TENS_{AS}$) is around 1340 MPa, it increases after the stress relieving treatment ($TENS_{RHT}$) and is maintained by the firing cycle (1440 MPa for $TENS_{CHT}$). Accordingly, hardness increases from about 73 HRA, for the $TENS_{AS}$ group, to about 76 HRA for the $TENS_{CHT}$ group (Table 4). On the contrary, the elongation at break (ε_b) shows the highest value for the $TENS_{AS}$ group, decreases after the RHT process and reaches its lowest value of 4.7 % for the $TENS_{CHT}$ group of samples (Table 4).

Table 4 about here

Results for the flexural specimens are listed in Table 5. Transverse rupture strength in the CHT state ($FLEX_{CHT}$) is as high as 2500 MPa, just slightly lower than after the sole relieving treatment ($FLEX_{RHT}$).

Table 5 about here

Results of statistical tests relating mechanical properties of TENS and FLEX groups of samples are reported in Table 6 in terms of p-value, estimated by the statistical software, as described above. It is evident from Table 6 that the relieving treatment makes the alloy stronger and more fragile ($TENS_{AS}$ – $TENS_{RHT}$). On the other hand, the firing cycle causes significant increase of hardness and loss of ductility, but leaves the alloy strength unchanged ($TENS_{CHT}$ – $TENS_{RHT}$).

Comparison of the results obtained for tensile and flexural tests, reported in the last rows of Table 6, evidences an almost identical behaviour.

Table 6 about here

3.3 Rupture surfaces

Figure 3 allows comparing the rupture surfaces of $TENS_{AS}$ samples with samples submitted to stress relieving treatment and firing cycle ($TENS_{CHT}$). Signs of ductile failure modes can be observed in the $TENS_{AS}$ sample (Figure 3a). Areas of ductile failure surround "quasi-cleavage" facets to which are added, on the facets themselves, surface irregularities that can be ascribed to shear failure (Figure 3a). Ductile failure modes disappear after the heat treatments (Figure 3b), where "quasi-cleavage" mechanisms take up the whole surface, together with many cracks (dotted lines in Figure 3b).

Figure 3 about here

3.3 X-ray Diffraction (XRD)

In order to follow the structural modifications induced on the material by the production process and the subsequent heat treatments, XRD investigations were carried out on the following samples: a) the metallic EOS CobaltChrome SP2 powder, b) the as sintered (AS) sample and c) the sintered sample submitted to the relieving and firing thermal treatments (CHT). Results of XRD measurements performed on the metallic powder have been already discussed in a previous paper (Barucca et al. 2015). Metallic powder is entirely composed of γ-Co (fcc) phase with an estimated lattice parameter a=0.3586±0.0002 nm (Barucca et al. 2015).

In Figure 4 XRD patterns of as sintered (AS) and heat-treated (CHT) samples are reported for comparison. Both samples are formed of a mixture of the ε-Co (hcp, a=0.25031 nm, c=0.40605 nm, ICDD card n. 5-727) and γ-Co (fcc, a=0.35447, ICDD card n. 15-806) phases. However, in the XRD pattern of the CHT sample in addition to the diffraction peaks of the ε-Co and γ-Co phases, low intensity peaks (evidenced by full dots in Figure 4) are visible.

Figure 4 about here

Quantitative information on the crystallographic structure of the ε-Co and γ-Co phases as well as their relative volume fraction were obtained by peak analysis of the two XRD patterns reported in Figure 4. The results of peak analysis are summarised in Table 7, where the experimental results obtained for the metallic powder, already discussed in our previous paper (Barucca et al. 2015), are reported for comparison.

Table 7 about here

The lattice parameters of the ε-Co and γ-Co phases were estimated from the angular position of the diffraction peaks. On the contrary, the volume fraction of the hcp phase (f_{hcp}) was calculated from the integrated intensities of the γ (200) and ε (101) peaks by using the method by Saude and Gillaud (Balagna et al. 2012). The experimental uncertainties in Table 7 were calculated from the statistical errors provided by the peak analysis software. The peak analysis of the low intensity peaks (evidenced by full dots in Figure 4) in the CHT pattern of Figure 4 suggest the formation of an hcp compound with estimated lattice parameters a=0.4734±0.0002 nm and c=0.7661±0.0003 nm.

3.4 Transmission electron microscopy (TEM, STEM, HRTEM) and microanalysis (EDX)

TEM observations of the AS and CHT samples confirm the simultaneous presence of the ε-Co and γ-Co phases. In both samples, the two phases give rise to a peculiar structure formed of alternating ε-Co and γ-Co lamellae. Figure 5 shows the lamellar structure in both samples.

Figure 5 about here

Figure 5a is a TEM bright field image of the AS sample taken in $<110>_{\gamma}$ zone axis orientation. Lamellae are parallel to each other with a width ranging from 5 to 100 nm. The corresponding selected area electron diffraction (SAED) pattern of the AS sample is shown in the inset of Figure 5a. The lattice cells due to the fcc γ-phase (dashed line) and to the hcp ε-phase (dotted line) are evidenced in the SAED pattern in Figure 5a. Relative orientation of the two lattice cells allows deducing the following Shoji-Nishiyama (Nishiyama 1978) orientation relationships between the ε-Co and γ-Co lamellae:

$$\{001\}_{\varepsilon} // \{111\}_{\gamma}$$

$$<100>_{\varepsilon} // <1\text{-}10>_{\gamma}$$

For comparison, an HRTEM image of the CHT sample is shown in Figure 5b. Also in this case, the lamellar structure is clearly visible. A Fourier analysis (FFT) performed on different regions (squares in Figure 5b) of two adjacent lamellae allowed obtaining the diffraction patterns reported in the insets of Figure 5b. The inset in the upper left corner shows the diffraction pattern of the fcc γ-Co phase (lattice cell evidenced by dashed line). On the contrary, the inset in the lower right corner of Figure 5b is the diffraction pattern of the hcp ε-Co phase with the lattice cell evidenced by dotted line. From the two diffraction patterns, one can conclude that the orientation relationships between the ε-Co and γ-Co adjacent lamellae in the CHT sample are unaltered with respect to the AS sample. Concerning average size of lamellae, TEM observations evidenced a slightly increase in the CHT sample with width now ranging from 10 to 120 nm.

The most evident effect induced by the thermal treatments performed on the Co alloy under study regard number and density of precipitates. Figure 6 shows the precipitates distribution in the AS (Figure 6a) and CHT (Figure 6b) samples, respectively.

Figure 6 about here

From the STEM - HAAD images of Figure 6 can be appreciated the larger amount of precipitates present in the CHT sample (Figure 6b) in comparison to the AS one (Figure 6a).

In Figure 6a (AS sample) two main types of precipitates are visible: coarse (bright) and small spherical (dark) precipitates. On the contrary, in Figure 6b (CHT sample) three different shapes can be distinguished: coarse (bright), small spherical (dark) and elongated (bright) precipitates. In the AS sample (Figure 6a) size of coarse precipitates ranges from 40 to 100 nm, while spherical dark ones have an average size of 10 nm and are often associated to coarse precipitates. In the CHT sample (Figure 6b) coarse precipitates range from 60 to 250 nm, elongated precipitates have length between 125 and 440 nm and the average size of small spherical ones is 13 nm. Small spherical precipitates also in the CHT sample are often associated to coarser ones.

EDX analysis performed during TEM and STEM observations allowed studying the chemical composition of the different precipitates. An elemental mapping analysis of the CHT sample performed by EDX signals of Si, Cr, Co, Mo and W is reported in Figure 7.

Figure 7 about here

It is evident from Figure 7 that coarse and elongated precipitates have almost the same composition while small spherical precipitates are mainly composed of Si even when they are associated to coarser ones. With respect to the Co matrix, coarse and elongated precipitates reveal a higher concentration of Mo and W.

Quantitative results of the EDX analysis performed on matrix and on a large number of coarse, elongated and spherical precipitates are shown in Table 8, where the average experimental concentration value for each element is reported with the corresponding standard deviation.

Table 8 about here

In order to further investigate the nature of coarse and elongated precipitates, SAED analyses and HRTEM observations were carried out on a number of different precipitates. The results obtained are summarised in Figure 8.

Figure 8 about here

Figure 8a shows a TEM bright field image of a coarse precipitate with the corresponding SAED pattern (inset). On the contrary, the HRTEM image of a coarse precipitate is reported in Figure 8b together with the FFT pattern (inset) obtained from the area of sample enclosed in the square. Crystallographic information deduced from SAED and FFT patterns in Figure 8 suggest an hcp structure of the coarse precipitate. Similar results obtained also for the elongated precipitates suggest a substantial identical crystallographic structure (hcp) for differently shaped precipitates.

Small spherical precipitates, often associated to coarser ones, are Si-rich inclusions already reported in literature (Giacchi et al. 2012).

4. Discussion

The Co-based material considered in this study is a typical low carbon alloy specifically developed by EOS GmbH Electro Optical System for biomedical applications (Table 2).

The metallic powder used as raw material for production of samples is entirely composed of the γ-Co (fcc) phase in form of spherical particles with size ranging from 4 to 80 μm (Barucca et al. 2015). The laser sintering process, carried out by using the sintering parameters shown in Table 1, melts the metallic powder and induces the martensitic γ-Co (fcc) $\rightarrow$ ε-Co (hcp) transformation (Saldivar-Garcia et al. 1999a, 1999b; Song et al. 2006). After solidification, the as-sintered (AS) sample is compact without any visible surface porosity. It is worth to note that the average roughness of all analysed samples shows an unexpected constant value, independently on the post-production treatment.

In terms of microstructure, the AS sample shows a mixture of martensitic ε-Co (hcp) inside the metastable γ-Co (fcc) phase (Figure 4), with a volume fraction of the ε-Co (hcp) phase around 49% (Table 7). Lattice parameters of γ-Co (fcc) and ε-Co (hcp) phases in metal powder and AS sample (Table 7), estimated from the XRD patterns, are in close agreement with values reported in literature for similar compositions (Saldivar-Garcia and Lopez 2004). Furthermore, TEM observation of the AS sample shows ε-Co (hcp) phase forming an intricate network of small lamellae in γ-Co (fcc) matrix (Figure 5a), while SAED pattern (inset in Figure 5a) confirms the Shoji-Nishiyama (SN) orientation relationships between the two Co phases (Nishiyama 1978). The particular orientation relationships (SN) developed are responsible of the mechanical properties observed in the AS sample (Table 4) (Barucca et al. 2015). The SN orientation relationships are typically observed in Co alloys submitted to fatigue deformation where the strain-induced γ-Co (fcc) → ε-Co (hcp) martensitic transformation plays a prominent role (Koizumi et al. 2013; Mitsunobu et al. 2014; Yamanaka et al 2014).

The stress relieving thermal treatment (RHT) carried out on AS samples just after the shot peening process induces modifications in the mechanical response of samples. From Table 4 it is evident that the alloy becomes harder and less ductile, with elongation at break decreasing from 9 to 6 %. Results of the t-test, listed in Table 6, further confirm the significant effect of the relieving treatment in making the alloy stronger and more fragile.

Further modifications in the mechanical behaviour of the alloy are evident after the firing cycle. Although the firing operation leaves strength unchanged, it causes additional significant rise in hardness and loss in ductility (Tables 4 and 6). Nevertheless, the final properties are, overall, well above those expected from the datasheet, in terms of both UTS and ε_b (compare Tables 3 and 4).

Flexural tests of CHT and RHT samples show a slightly different behaviour with respect to tensile specimens (Table 5). In fact, while tensile strength is substantially unaffected by the firing cycle (Table 4), flexural strength decreases, by approximately 7% (Table 5), with a statistical significance

just barely below the 0.05 threshold (Table 6). The last rows in Table 6 refer to t-test for hardness values, when tensile and flexural specimens subjected to the same treatment are compared. Results for p-values high above the level of 0.05 prove that tensile and flexural specimens are undifferentiated.

Modifications of the mechanical behaviour are strictly linked to structural changes induced by RHT and CHT thermal treatments. As shown in Figure 4 and quantitatively reported in Table 7, heat treatments tend to stabilize the amount of martensitic ε-Co (hcp) phase (volume fraction increases from about 50% in the SA sample to 63% in the CHT state) as well as to induce formation of a hexagonal compound not present in the AS condition.

Increase of total amount of martensitic ε-Co (hcp) phase in the CHT sample is accompanied by a limited increase of the size of ε-Co lamellae while the orientation relationships between ε-Co and γ-Co lamellae remain unaltered (Figure 5). Furthermore, XRD investigations (not reported here) performed in the unstrained shoulder and in proximity of highly strained gage region of the $TENS_{AS}$ sample evidenced a volume fraction increase of the martensitic ε-Co (hcp) phase from about 50% to about 65%, totally ascribable to strain induced martensitic transformation (Koizumi et al. 2013; Mitsunobu et al. 2014). It is worth to note that this latter result spans the same interval values of the martensitic transformation induced by heat treatments. Thus, volume fraction increase of the martensitic phase as well as slight size increase of its lamellar structure cannot fully justify the observed variations of mechanical response between AS and CHT samples.

On the other side, TEM/STEM observations evidenced in the CHT sample a massive formation of coarse and elongated precipitates (Figure 6b) having identical chemical composition (Table 8) independently of their own shape. The uniformity of composition is further confirmed in the EDX elemental mapping of Figure 7 where differently shaped precipitates show the same contrast level (same colour). Furthermore, HRTEM investigations evidenced an identical hcp crystallographic structure for both coarse and elongated precipitates (Figure 8).

As far as the chemical composition of both coarse and elongated precipitates is concerned, it must be stressed that, with respect to matrix, the Mo and W content in the precipitates highly increases while the Si amount undergoes a more limited variation (Table 8). Chemical databases such as International Centre for Diffraction Data (The International Centre for Diffraction Data (ICDD), 12 Campus Boulevard, Newtown Square, PA 19073-3273 U.S.A., http://www.icdd.com) and Mat Navi (NIMS Materials Database – Inorganic Materials Database, Atom Work) (Xu et al. 2011) report two possible compounds compatible with the above crystallographic structure and elements content: a) a molybdenum-containing phase Co_3Mo_2Si, hcp with a=0.47 nm and c=0.767 nm (ICDD card n. 30-449), and b) a tungsten-containing phase $WCo_{1.5}Si_{0.5}$, hcp with a=0.4718 nm and c=0.76 nm (Atom Work). Therefore, crystallographic and compositional results suggest that the post-production treatments are responsible of formation and growth of coarse and elongated precipitates having an hcp structure, with lattice parameters a=0.4734±0.0002 nm and c=0.7661±0.0003 nm and a composition resembling $Co_3(Mo,W)_2Si$, with possible interchange of Mo and W atoms in the crystallographic lattice. To our better knowledge, the presence of such coarse and elongated precipitates is reported here for the first time.

Actually, a number of paper in literature report the presence of precipitates with various morphology (blocky, star-like, lamellar) in biomedical Co-Cr alloys produced by conventional processes. In particular, the contemporary presence of differently shaped precipitates was clearly evidenced while chemical extraction techniques allowed their detailed crystallographic and compositional characterisation (Mineta et al. 2010; Alfirano et al. 2011). A complete review of morphology and composition of precipitates observed thus far in Co-Cr biomedical alloys is reported in the paper by Narushima et al. (2013) where the influence of alloying elements such as carbon, nitrogen, silicon and manganese is also investigated. Always from this paper, it follows that precipitates with identical or similar composition can occur in the same alloy with different morphologies.

On the contrary, the chemical composition and the crystallographic structure of the coarse and elongated precipitates observed here do not match any known phase already reported in literature for

biomedical Co-Cr-W systems (Narushima et al. 2013). Although this latter result can be almost completely ascribed to the chemical composition of our alloy (Table 2), it cannot be excluded some influence of the laser sintering production process.

The presence of isolated Si inclusions or associated to larger precipitates, typically carbides in carbon containing alloys, is well known in literature (Yamanaka et al. 2015; Giacchi et al. 2011, 2012). As evident in Figures 6 and 7, in our case Si inclusions, the small dark spherical particles, form as isolated precipitates or, more frequently, associated to both coarse and elongated precipitates. It cannot be excluded that Si inclusions can have a role in nucleation and growth of coarse and elongated precipitates.

The rupture surfaces shown in Figure 3 contribute to explain the change in the mechanical response due to the heat treatments, towards a stronger and more fragile behaviour. Final microstructure exhibits clear signs of fragile failure modes and diffused cracks (Figure 3b), which is consistent with precipitates acting as stress intensifiers and crack initiators. In addition, the decrease of γ-Co (fcc) lattice parameters from AS to CHT condition (Table 7) suggests that the contraction trend of the matrix may be hampered by the presence of precipitates. Consequently, this would cause a tensile stress state in the matrix.

Summarising the complete set of results, one can conclude that high strength and hardness values measured in AS condition are mainly due to the intricate network of ε-Co (hcp) lamellae formed in the γ-Co (fcc) matrix during sintering and solidification processes (Barucca et al. 2015). On the contrary, total amount and size of martensitic lamellae seem to have a limited influence on modifications of the alloy mechanical response observed between AS and CHT states. In this case, the main variations of the mechanical behaviour can be ascribed to formation and growth of coarse and elongated precipitates that takes place during the stress relieving heat treatment and the subsequent firing cycle.

Conclusions

A Co-Cr-Mo-W alloy specifically developed for biomedical applications has been produced by Direct Metal Laser Sintering (DMLS). In order to investigate the effects of complex post-production treatments, the alloy was submitted to shot-peening, stress relieving and firing treatments. Temperature values as high as 950 °C were reached during the thermal treatments causing modifications of alloy microstructure and mechanical behaviour. The main results obtained in this study can be summarised as follows:

- samples are compact without any visible porosity with an average surface roughness value independent on the post-production treatment;
- the as-sintered sample is formed of an intricate network of ε-Co (hcp) lamellae in the γ-Co (fcc) matrix responsible of the high UTS and hardness values. Rupture surfaces evidence ductile failure modes;
- the stress relieving treatment (RHT) increases both UTS and hardness while decreases ductility;
- the firing cycle performed after the RHT treatment produces a further loss in ductility and a significant hardness increase while leaving strength unchanged. The alloy microstructure is still formed of slightly grown ε-Co (hcp) lamellae in the γ-Co (fcc) matrix to which superimposes a massive precipitation of coarse and elongated precipitates, which are reported here for the first time, and small spherical Si-rich inclusions. Quasi-cleavage mechanisms and cracks are evident from the rupture surfaces;
- XRD investigations carried out in conjunction with TEM/STEM/HRTEM observations and EDX analysis show that the coarse and elongated precipitates observed here for the first time have a hcp structure with lattice parameters a=0.4734±0.0002 nm and c=0.7661±0.0003 nm and a possible composition resembling $Co_3(Mo,W)_2Si$.

Complex post-production treatments eventually associated to strain-induced γ-Co (fcc) → ε-Co (hcp) martensitic transformation can be used to induce structural modifications capable of producing controlled changes in the mechanical response of laser sintered Co-Cr-Mo-W biomedical alloys.

Acknowledgements

The research leading to these results has received funding from the European Union Seventh Framework Programme under grant agreement 312483 - Esteem2 (integrated infrastructure initiative–I3). The authors kindly acknowledge MSc. Adam Gruszczynski (AGH-UST) and A. Di Cristoforo (UNIVPM) for FIB lamellae and TEM sample preparation.

References

Alfirano, Mineta, S., Namba, S., Yoneda, T., Ueda, K., Narushima, T., 2011. Precipitates in as-cast and heat-treated ASTM F75 Co-Cr-Mo-C alloys containing Si and/or Mn. Met. Mat. Trans. A 42, 1941-1949.

Al Jabbari, Y.S., Koutsoukis, T., Barmpagadaki, X., Zinelis, S., 2014. Metallurgical and interfacial characterization of PFM Co–Cr dental alloys fabricated via casting, milling or selective laser melting. Dent. Mat. 30, e79–e88.

Antunes, R.A., Lopes de Oliveira, M.C., 2012. Corrosion fatigue of biomedical metallic alloys: Mechanisms and mitigation. Acta Biomat. 8, 937–962.

Balagna, C., Spriano, S., Faga, M.G., 2012. Characterization of Co-Cr-Mo alloy after a thermal treatment for high wear resistance. Mat. Sci. Eng. C 32, 1868-1877.

Barucca, G., Santecchia, E., Majni, G., Girardin, E., Bassoli, E., Denti, L., Gatto, A., Iuliano, L., Moskalewicz, T., Mengucci, P., 2015. Structural characterization of biomedical Co–Cr–Mo components produced by direct metal laser sintering. Mat. Sci. Eng. C 48, 263–269.

Bassoli, E., Gatto, A., Iuliano, L., 2012. Joining mechanisms and mechanical properties of PA composites obtained by selective laser sintering. Rapid Prot. J. 18, 100–108.

Bassoli, E., Sewell, N., Denti, L., Gatto, A.. 2013. Investigation into the failure of inconel exhaust collector produced by laser consolidation. Eng. Failure Analysis 35, 397–404.

Craig, R.G., Powers, J., Wataha, J., 2004. Dental Materials: Properties and Manipulation, 8th edition, Mosby, St Louis.

Frazier, W.E., 2014. Metal additive manufacturing: A review. J. Mat. Eng. Perf. 23, 1917-1928.

Giacchi, J.V., Morando, C.N., Fornaro, O., Palacio, H.A., 2011. Microstructural characterization of as-cast biocompatible Co–Cr–Mo alloys. Mat. Char. 62, 53-63.

Giacchi, J.V., Fornaro, O., Palacio, H.A., 2012. Microstructural evolution during solution treatment of Co–Cr–Mo–C biocompatible alloys. Mat. Char. 68, 49-57.

Harris, I.D., 2012. Additive manufacturing: A transformational advanced manufacturing technology. Adv. Mat. Proc. 5, 25–29.

Hedberg, Y.S., Qian, B., Shen, Z., Virtanen, S., Odnevall-Wallinder, I., 2014. In vitro biocompatibility of CoCrMo dental alloys fabricated by selective laser melting. Dent. Mat. 30, 525–534.

Hiromoto, S., Onodera, E., Chiba, A., Asami, K., Hanawa, T., 2005. Microstructure and corrosion behaviour in biological environments of the new forged low-Ni Co–Cr–Mo alloys. Biomaterials, 26, 4912-4923.

Koizumi, Y., Suzuki, S., Yamanaka, K., Lee, B.S., Sato, K., Li, Y., Kurosu, S., Matsumoto, H., Chiba, A., 2013. Strain-induced martensitic transformation near twin boundaries in a biomedical Co–Cr–Mo alloy with negative stacking fault energy. Acta Mat. 61, 1648–1661.

Lu, Y., Wu, S., Gan, Y., Li, J., Zhao, C., Zhuo, D., Lin, J., 2015. Investigation on the microstructure, mechanical property and corrosion behavior of the selective laser melted CoCrW alloy for dental application. Mat. Sci. Eng. C 49, 517–525.

Madl, A.K., Liong, M., Kovochich, M., Finley, B.L., Paustenbach, D.J., Oberdörster, G., 2015. Toxicology of wear particles of cobalt-chromium alloy metal-on-metal hip implants Part I:

Physicochemical properties in patient and simulator studies. Nanomed.: Nanotech. Biol. Med. 11, 1201–1215.

Mineta, S., Namba, S., Yoneda, T., Ueda, K., Narushima, T., 2010. Carbide formation and dissolution in biomedical Co-Cr-Mo alloys with different carbon contents during solution treatment. Met. Mat. Trans. A 41, 2129-2138.

Mitsunobu, T., Koizumi, Y., Lee, B.S., Yamanaka, K., Matsumoto, H., Li, Y., Chiba, A., 2014. Role of strain-induced martensitic transformation on extrusion and intrusion formation during fatigue deformation of biomedical Co–Cr–Mo–N alloys. Acta Mat. 81, 377-385.

Mostardi, R.A., Kovacik, M.W., Ramsier, R.D., Bender, E.T., Finefrock, J.M., Bear, T.F., Askew, M.J., 2010. A comparison of the effects of prosthetic and commercially pure metals on retrieved human fibroblasts: The role of surface elemental composition. Acta Biomat. 6, 702–707.

Mumtaz, K.A., Erasenthiran, P., Hopkinson, N., 2008. High density selective laser melting of Waspaloy. J. Mat. Proc. Tech. 195, 77-83.

Narushima, T., Mineta, S., Kurihara, Y., Ueda, K., 2013. Precipitates in biomedical Co-Cr alloys. JOM: The Journal of The Minerals, Metals & Materials Society (TMS) 65, 489-504.

Nishiyama, Z., 1978. Martensitic transformations, Editors: M. Fine, M. Meshii, C. Wayman, Academic Press, London.

Saldıvar-Garcıa, A.J., Manı-Medrano, A., Salinas-Rodrıguez, A., 1999a. Effect of solution treatments on the fcc/hcp isothermal martensitic transformation in Co-27Cr-5Mo-0.05C aged at 800°C. Scripta Mat. 40, 717-722.

Saldıvar-Garcıa, A.J., Manı-Medrano, A., Salinas-Rodrıguez, A., 1999b. Formation of hcp martensite during the isothermal ageing of an fcc Co-27Cr-5Mo-0.05C orthopaedic implant alloy. Met. Mat. Trans. A 30, 1177-1184.

Saldivar-Garcia, A.J., Lopez, H.F., 2004. Temperature effects on the lattice constants and crystal structure of a Co–27Cr–5Mo low-carbon alloy. Metall. Mat. Trans. A 35, 2517–2523.

Saldivar-Garcia, A.J., Lopez, H.F., 2005. Microstructural effects on the wear resistance of

wrought and as-cast Co–Cr–Mo–C implant alloys. J. Biomed. Mater. Res. 74A, 269-274.

Sanz, C., Navas, V.G., 2013. Structural integrity of direct metal laser sintered parts subjected to thermal and finishing treatments. J. Mat. Proc. Tech. 213, 2126-2136.

Simchi, A., 2006. Direct laser sintering of metal powders: Mechanism, kinetics and microstructural features. Mat. Sci. Eng. A 428, 148–158.

Stadelmann, P., 2007. JEMS: Java Electron Microscopy Software. Available from: http://cime. epfl.ch.

Stamp, R., Fox, P., O'Neill, W., Jones, E., Sutcliffe, C., 2009. The development of a scanning strategy for the manufacture of porous biomaterials by selective laser melting. J. Mat. Sci. Mat. Med. 20, 1839-1848.

Song, C.B., Park, H.B., Seong, H.G., Lopez, H.F., 2006. Development of athermal ε-martensite in atomized Co-Cr-Mo-C implant alloy powders. Acta Biomat. 2, 685-691.

Takaichi, A., Suyalatu, Nakamoto, T., Joko, N., Nomura, N., Tsutsumi, Y., Migita, S., Doi, H., Kurosu, S., Chiba, A., Wakabayashi, N., Igarashi, Y., Hanawa, T., 2013. Microstructures and mechanical properties of Co–29Cr–6Mo alloy fabricated by selective laser melting process for dental applications. J. Mech. Beav. Biomed. Mat. 21, 67–76.

Ucar, Y., Akova, T., Akyil, M., Brantley, W.A., 2009. Internal fit evaluation of crowns prepared using a new dental crown fabrication technique: laser-sintered Co-Cr crowns. J. Prost. Dent. 102, 253-259.

Wataha, J.C., 2002. Alloys for prosthodontic restorations. J. Prost. Dent. 87, 351–363.

Xin, X.Z., Xiang, N., Chen, J., Wei, B., 2012. In vitro biocompatibility of Co–Cr alloy fabricated by selective laser melting or traditional casting techniques. Mat. Letters 88, 101–103.

Xin, X.Z., Chen, J,, Xiang, N., Gong, Y., Wei, B., 2014. Surface characteristics and corrosion properties of selective laser melted Co–Cr dental alloy after porcelain firing. Dent. Mat. 30, 263-270.

Xu, Y., Yamazaki, M., Villars, P., 2011. Inorganic Materials Database for Exploring the Nature of Material. Jpn. J. Appl. Phys. 50, 11RH02.

Yamanaka, K., Mori, M., Chiba, A., 2013. Nanoarchitectured Co–Cr–Mo orthopedic implant alloys: Nitrogen enhanced nanostructural evolution and its effect on phase stability. Acta Biomat. 9, 6259-6267.

Yamanaka, K., Mori, M., Koizumi, Y., Chiba, A., 2014. Local strain evolution due to athermal γ-ε martensitic transformation in biomedical Co–Cr–Mo alloys. J. Mech. Behav. Biomed. Mat. 32, 52–61.

Yamanaka, K., Mori, M., Chiba, A., 2015. Assessment of precipitation behaviour in dental castings of a Co–Cr–Mo alloy. J. Mech. Behav. Biomed. Mat. 50, 268–276.

Yoda, K., Suyalatu, Takaichi, A., Nomura, N., Tsutsumi, Y., Doi, H., Kurosu, S., Chiba, A., Igarashi, Y., Hanawa, T., 2012. Effects of chromium and nitrogen content on the microstructures and mechanical properties of as-cast Co–Cr–Mo alloys for dental applications. Acta Biomat. 8, 2856-2862.

Zangeneh, S., Lashgari, H.R., Saghafi, M., Karshenas, M., 2010. Effect of isothermal aging on the microstructural evolution of Co–Cr–Mo–C alloy. Mat. Sci. Eng. A 527, 6494-6500.

Figure and table captions

Table 1 Standard sintering parameters used for DMLS

Table 2 Nominal powder composition (wt%)

Table 3 Physical and mechanical properties in the material datasheet, after stress relieving, oxide fire simulation (5 min at 950 °C) and ceramic fire simulation (4 x 2 min at 930 °C) procedures according to EN ISO 22674.

Table 4 Average value (AV) and standard deviation (SD) of ultimate tensile strength (UTS), strain at break (ε_b) and Rockwell A hardness (HRA) of the tensile specimens (TENS) under different condition.

Table 5 Average value (AV) and standard deviation (SD) of Rockwell A hardness (HRA) and transverse rupture strength (TRS) of the flexural specimens.

Table 6 p-values resulting from the t-test for UTS, ε_b, HRA and TRS among the groups AS, RHT and CHT. Records below the level of significance of 0.05 are underlined.

Table 7 Experimental results of the peak analysis performed on the XRD spectra of Figure 4. The estimated lattice parameter of the γ-Co phase in the powder is reported for comparison.

Table 8 Results of STEM-EDX analysis performed on matrix and precipitates. Element concentration in wt%.

Figure 1 Geometry of samples for mechanical tests: a) flexural (FLEX), b) tensile (TENS).

Figure 2 Thermal cycle used for fire simulation. The cooling phase between each firing step is not represented.

Figure 3 SEM images of rupture surface: a) $TENS_{AS}$, b) $TENS_{CHT}$.

Figure 4 XRD patterns of the as sintered (AS) and heat treated (CHT) samples.

Figure 5 TEM images taken in <110>$_\gamma$ zone axis orientation showing the lamellar structure of samples: a) AS sample – inset: corresponding SAED pattern, b) CHT sample – insets: Fourier analysis of the squared regions.

Figure 6 STEM images of the samples microstructure: a) AS condition, b) CHT condition.

Figure 7 STEM-EDX elemental mapping obtained with signals from Si, Cr, Co, Mo and W.

Figure 8 Coarse precipitates: a) TEM bright field and corresponding SAED pattern (inset), b) HRTEM image and corresponding FFT (inset) of the squared region.

Table 1

Table 1 Standard sintering parameters used for DMLS

laser power	200W
laser spot diameter	0.200 mm
Scan speed	up to 7.0 m/s
Building speed	2-20 mm^3/s
Layer thickness	0.020 mm
Protective atmosphere	max 1.5% oxygen

Table 2

Table 2 Nominal powder composition (wt%)

Co	Cr	Mo	W	Si	Fe	Mn
63.8	24.7	5.1	5.4	1.0	< 0.5	< 0.1

Table 3

Table 3 Physical and mechanical properties in the material datasheet, after stress relieving, oxide fire simulation (5 min at 950 °C) and ceramic fire simulation (4 x 2 min at 930 °C) procedures according to EN ISO 22674.

Coefficient of thermal expansion [K^{-1}]	$14.3 \cdot 10^{-6}$
Density [kg/dm^3]	8.5
UTS [MPa]	1350
$R_{p0.2}$ [MPa]	850
Elongation at break	3%
Young's Modulus [GPa]	200
HV10	420

Table 4

Table 4 Average value (AV) and standard deviation (SD) of ultimate tensile strength (UTS), strain at break (ε_b) and Rockwell A hardness (HRA) of the tensile specimens (TENS) under different condition.

	UTS (MPa)		ε_b (%)		HRA	
	AV	SD	AV	SD	AV	SD
$TENS_{AS}$	1340	20	9.0	0.8	72.8	1.8
$TENS_{RHT}$	1430	10	6.2	0.4	74.2	1.8
$TENS_{CHT}$	1440	20	4.7	0.3	75.8	1.5

Table 5

Table 5 Average value (AV) and standard deviation (SD) of Rockwell A hardness (HRA) and transverse rupture strength (TRS) of the flexural specimens.

	HRA		TRS (MPa)	
	AV	SD	AV	SD
$FLEX_{RHT}$	73.2	0.4	2700	25
$FLEX_{CHT}$	76.0	0.5	2500	157

Table 6

Table 6 p-values resulting from the t-test for UTS, ε_b, HRA and TRS among the groups AS, RHT and CHT. Records below the level of significance of 0.05 are underlined.

	p-values			
	UTS (MPa)	ε_b (%)	HRA	TRS
$TENS_{AS}$ -$TENS_{RHT}$	0.00	0.00	0.01	-
$TENS_{AS}$ - $TENS_{CHT}$	0.00	0.00	0.00	-
$TENS_{CHT}$ -$TENS_{RHT}$	0.13	0.00	0.00	-
$FLEX_{CHT}$ -$FLEX_{RHT}$	-	-	0.00	0.04
$TENS_{RHT}$ - $FLEX_{RHT}$	-	-	0.28	-
$TENS_{CHT}$ – $FLEX_{CHT}$	-	-	0.77	-

Table 7

Table 7 Experimental results of the peak analysis performed on the XRD spectra of Figure 4. The estimated lattice parameter of the γ-Co phase in the powder is reported for comparison.

Sample	**Lattice parameter (fcc) γ-Co (nm)**	**Lattice parameters (hcp) ε-Co (nm)**	**Volume fraction hcp f_{hcp}**
Powder	a= 0.3586±0.0002	-	-
AS	a= 0.3589±0.0001	a= 0.2539±0.0002 c= 0.415±0.003 c/a= 1.636	0.49±0.03
CHT	a= 0.3574±0.0006	a= 0.2534±0.0004 c= 0.408±0.002 c/a= 1.612	0.625±0.005

Table 8

Table 8 Results of STEM-EDX analysis performed on matrix and precipitates. Element concentration in wt%.

	Co	**Cr**	**Mo**	**W**	**Si**
Matrix	64.7 ± 0.6	23.3 ± 0.2	3.2 ± 0.2	5.7 ± 0.5	3.16 ± 0.06
Coarse and elongated precipitates	36 ± 2	13± 2	21 ± 4	26 ± 3	5 ± 2
Spherical precipitates	24.8 ± 0.8	15.1 ± 0.6	1.7 ± 0.3	1.7 ± 0.1	56.7 ± 0.6

Figure 1

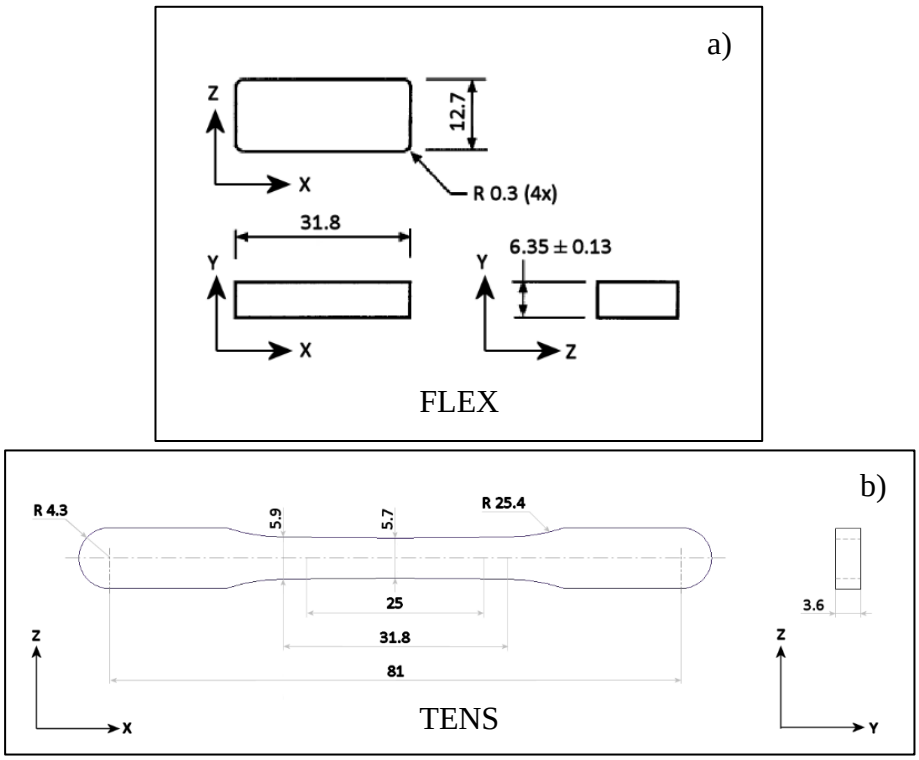

Figure 1 Geometry of samples for mechanical tests: a) flexural (FLEX), b) tensile (TENS).

Figure 2

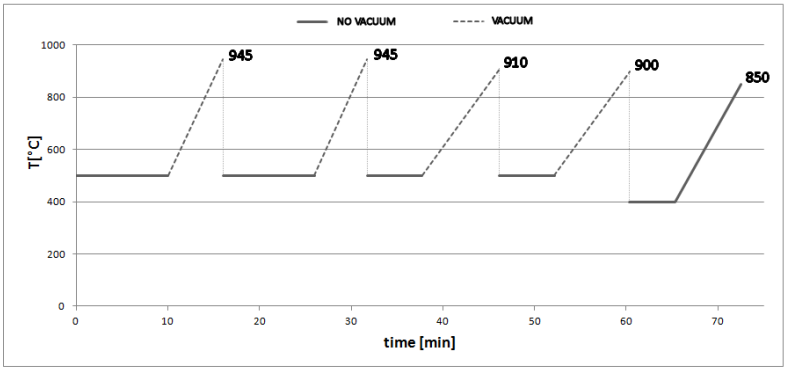

Figure 2 Thermal cycle used for fire simulation. The cooling phase between each firing step is not represented.

Figure 3

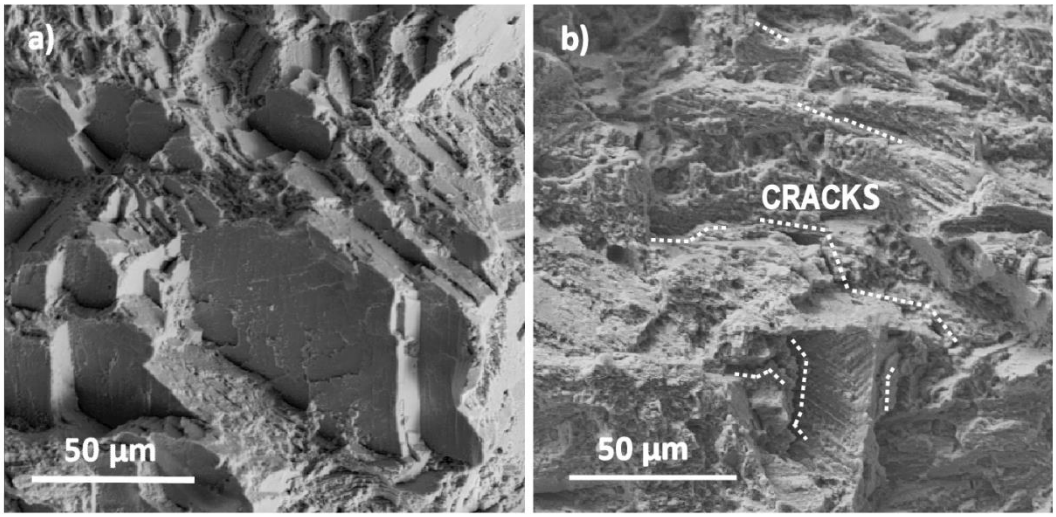

Figure 3 SEM images of rupture surface: a) $TENS_{AS}$, b) $TENS_{CHT}$.

Figure 4

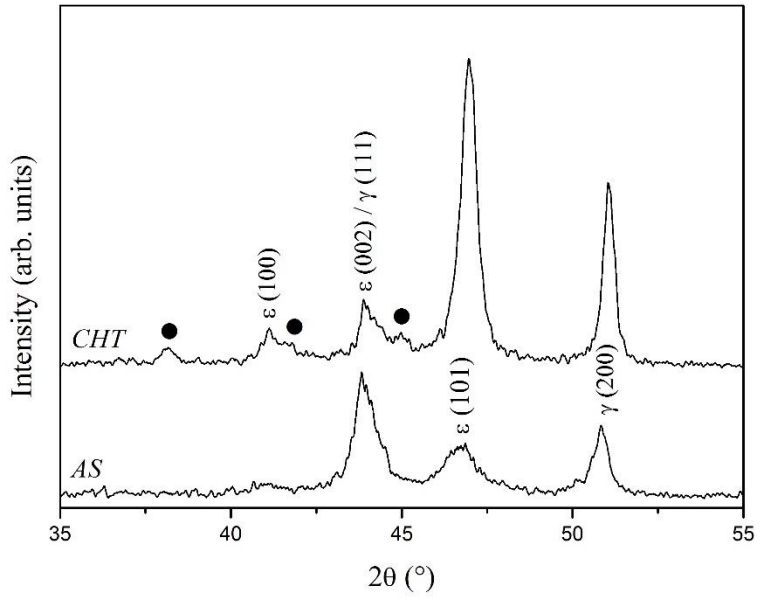

Figure 4 XRD patterns of the as sintered (AS) and heat treated (CHT) samples.

Figure 5

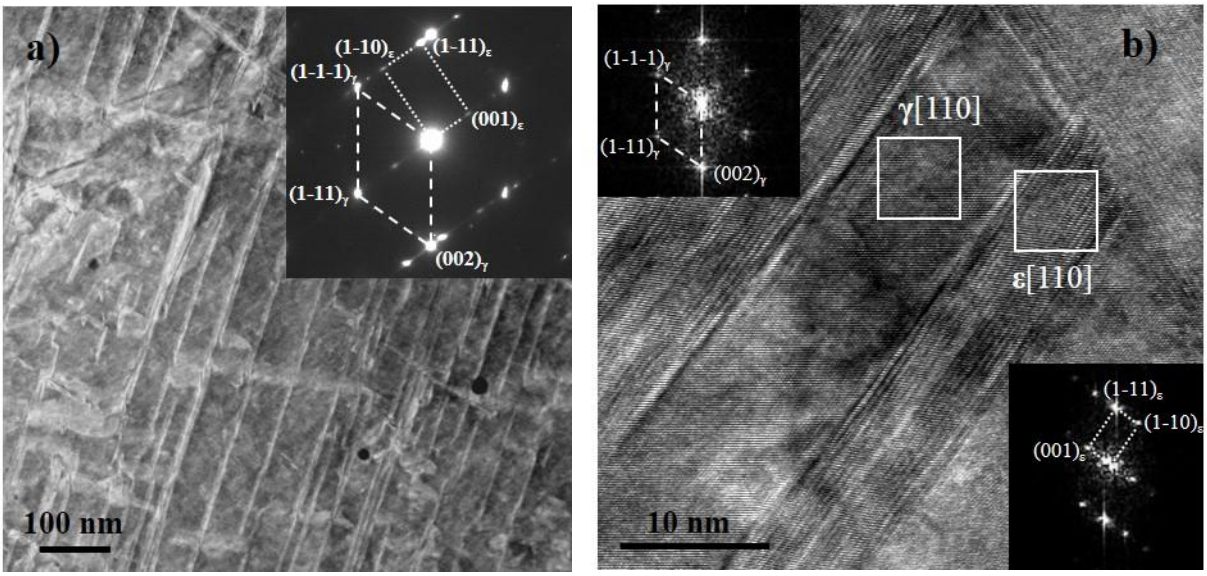

Figure 5 TEM images taken in <110>$_\gamma$ zone axis orientation showing the lamellar structure of samples: a) AS sample – inset: corresponding SAED pattern, b) CHT sample – insets: Fourier analysis of the squared regions.

Figure 6

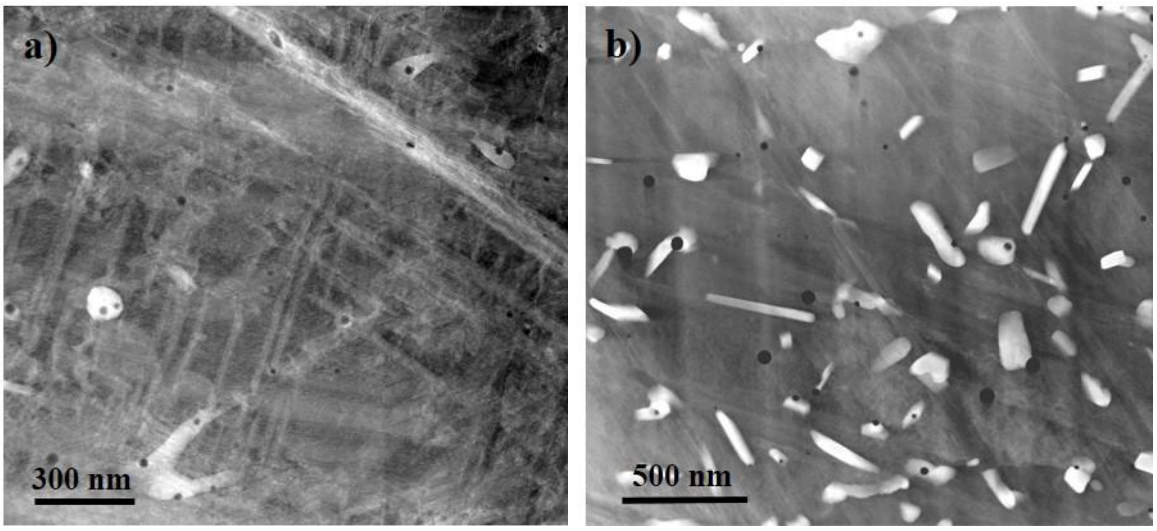

Figure 6 STEM images of the samples microstructure: a) AS condition, b) CHT condition.

Figure 7

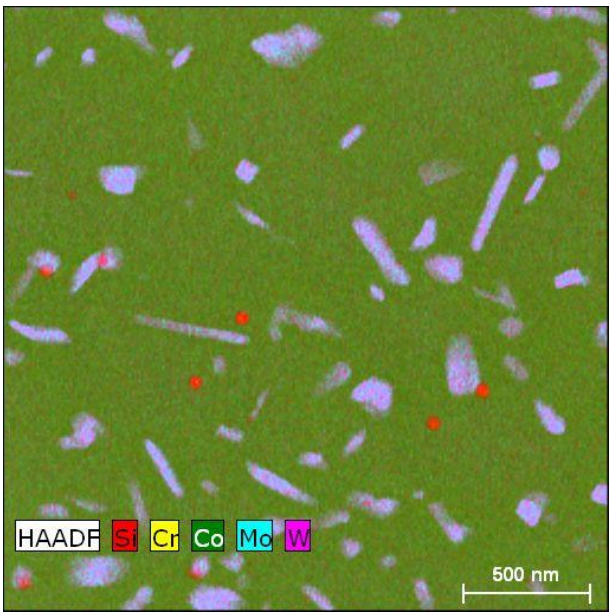

Figure 7 STEM-EDX elemental mapping obtained with signals from Si, Cr, Co, Mo and W.

Figure 8

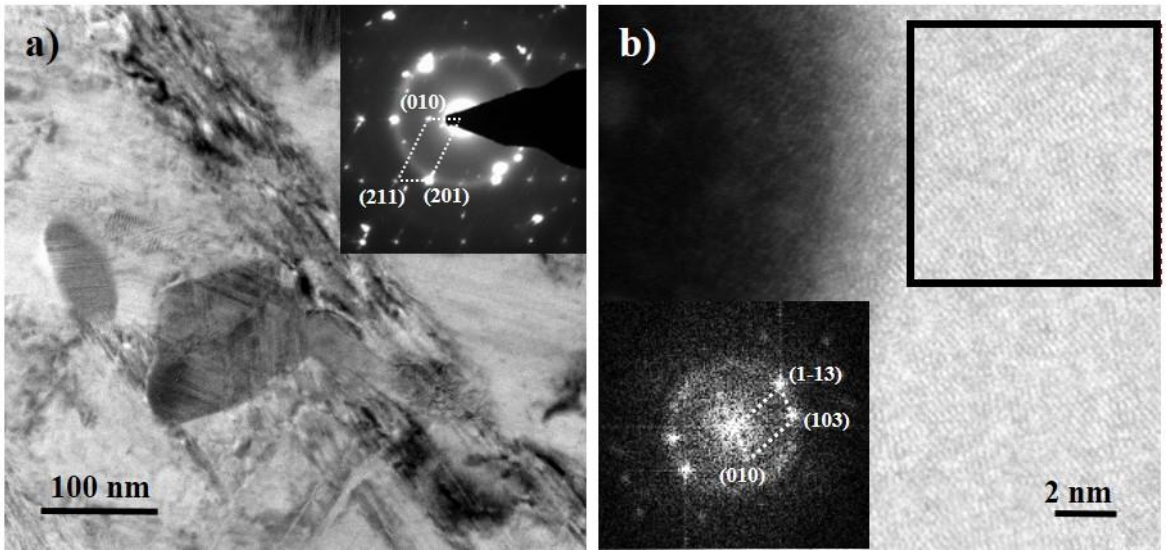

Figure 8 Coarse precipitates: a) TEM bright field and corresponding SAED pattern (inset), b) HRTEM image and corresponding FFT (inset) of the squared region.